SAND96-2236C
SAND--96-2236C

Localizing Heat-Generating Defects Using Fluorescent Microthermal Imaging

CONF-961180--1

RECEIVED
SEP 18 1996
OSTI

Paiboon Tangyunyong, Alan Y. Liang, Alan W. Righter*, Daniel L. Barton and Jerry M. Soden

Electronic Quality/Reliability Center
Sandia National Laboratories, Failure Analysis Department 1275, M/S 1081
Albuquerque, NM 87185-1081, USA
phone: (505) 844-3460, fax: (505) 844-2991
email: ptangyu@ sandia.gov
* MultiChip Module Applications Department 1277, M/S 1073

Abstract

Fluorescent microthermal imaging (FMI) involves coating a sample surface with a thin fluorescent film that, upon exposure to UV light source, emits temperature-dependent fluorescence [1-7]. The principle behind FMI was thoroughly reviewed at the ISTFA in 1994 [8, 9]. In two recent publications [10,11], we identified several factors in film preparation and data processing that dramatically improved the thermal resolution and sensitivity of FMI. These factors include signal averaging, the use of base mixture films, film stabilization and film curing. These findings significantly enhance the capability of FMI as a failure analysis tool. In this paper, we show several examples that use FMI to quickly localize heat-generating defects ("hot spots"). When used with other failure analysis techniques such as focused ion beam (FIB) cross sectioning and scanning electron microscope (SEM) imaging, we demonstrate that FMI is a powerful tool to efficiently identify the root cause of failures in complex ICs. In addition to defect localization, we use a failing IC to determine the sensitivity of FMI (i.e., the lowest power that can be detected) in an ideal situation where the defects are very localized and near the surface.

Experimental Setup, Film Preparation and Image Processing

All the measurements in this paper were performed using a Zeiss laser scanning microscope. A 200 watt mercury/xenon arc lamp and a band pass filter were used to provide a UV output between 365-400 nm. The fluorescent films was illuminated by the UV source in a coincident configuration (Fig. 1). A 612 nm interference filter was used to filter out all fluorescence except the dominant line at 612 nm. The 612 nm fluorescence of the sample was detected using a liquid-nitrogen-cooled, slow-scan, CCD camera that has a 512x512 pixel array. All the measurements were done with base mixture films. The base mixture solution consists of 1.2 wt% EuTTA (europium thenoyltrifluoroacetonate), 1.8 wt% PMMA (polymethyl-methacrylate), and 97 wt% MEK (methylethylketone) [1]. All films were prepared by applying a drop of solution onto each sample with an eye dropper. The films were then allowed to dry in air without spinning.

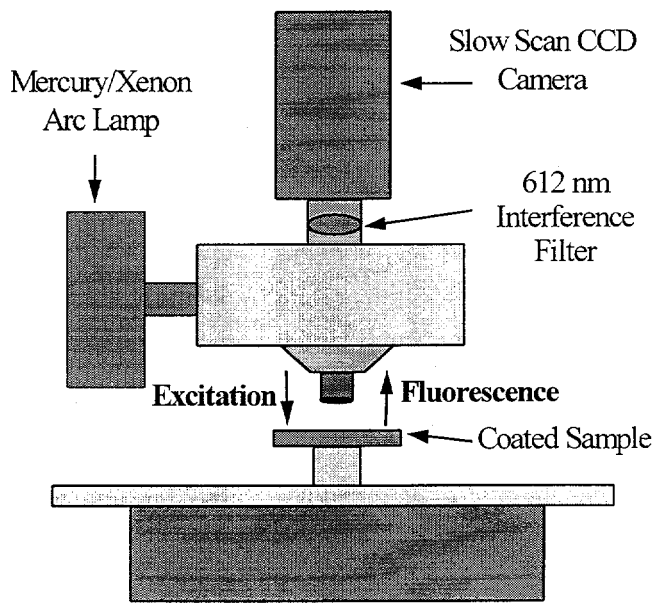

Fig. 1 - Schematic diagram showing the FMI setup with coincident illumination.

DISTRIBUTION OF THIS DOCUMENT IS UNLIMITED

MASTER

DISCLAIMER

Portions of this document may be illegible in electronic image products. Images are produced from the best available original document.

Thermal images were generated using image processing software to divide an image taken without bias (cold image) by one taken under bias (hot image). In this cold/hot image processing, hot areas in the resulting thermal image appear bright. The relative temperature change at a given location can be calculated by [1, 2]

$$\delta T \approx \alpha^{-1} \cdot \ln\left[\frac{Q(T_C)}{Q(T_H)}\right] = \alpha^{-1} \cdot \ln\left[\frac{S_C(x,y)}{S_H(x,y)}\right] \qquad (1)$$

where $Q(T_C)$, $S_C(x,y)$, $Q(T_H)$ and $S_H(x,y)$ are the quantum efficiency and photon intensity of the cold and hot images, respectively. The proportionality constant (α) was determined experimentally as described in reference 10 and was found to be 0.0245. For compatibility with our image processing software, a scale factor was used to keep the intensity ratio of the thermal image in the middle of the gray-scale range. Since our system acquired 16-bit images with a gray-scale range of 0 to 65535, a scale factor of 30000 was chosen.

Applications to Failure Analysis

Example 1. The first example is a 1-megabit CMOS SRAM. It is a 128K x 8 SRAM with a nominal operating voltage of 5 V and a standby I_{DDQ} of < 1 μA. It has an effective channel length (L_{eff}) of 0.5 μm (0.6 μm drawn), gate oxide thickness (t_{ox}) of 16 nm, 3 layers of metal and 2 layers of polysilicon. It was designed to be I_{DDQ}-testable [12]. The SRAM cell design is a standard six-transistor cell. After dynamic burn-in, the SRAM failed the functional test and had an elevated I_{DDQ} of 3 mA. As shown in the I-V curve in Fig. 2, the IC has low I_{DDQ} below 1 V. Above 1 V, the I-V curve shows a linear characteristic, indicating that the high I_{DDQ} is a result of a resistive short. As expected, no light emission was detected on this IC (resistive defects often do not have photon generation mechanisms). With FMI, two "hot spots" were quickly located (Fig. 3). Using SEM imaging and FIB cross sectioning (Figs. 4 & 5), the root cause of failure was identified to be an embedded particle that produced an ohmic short between two adjacent metal lines. The size of the particle estimated from the SEM image is ~ 5 μm in diameter. The resistance of the short was estimated to be ~ 1200 Ω based on the linear region of Fig. 2. The FIB cross section showed that the particle was encapsulated by a passivation layer, indicating the particle was most likely deposited onto the IC right after the last metal etching process but before the passivation step. Energy dispersive x-ray (EDX) analysis of the particle in Fig. 6 showed the presence of iron, nickel and chromium, indicating it was a stainless steel particle.

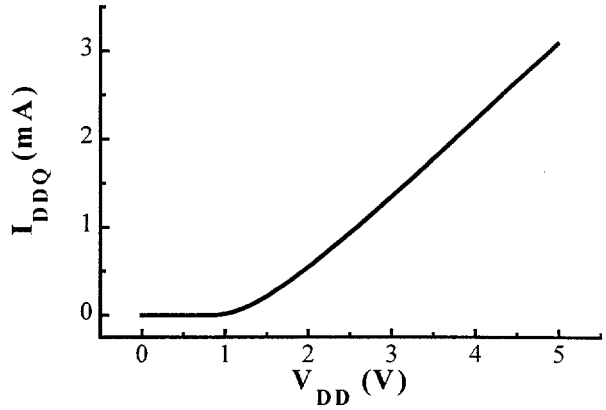

Fig. 2 - I_{DDQ} versus V_{DD} for the failed SRAM in example 1, showing a linear region above 1 V.

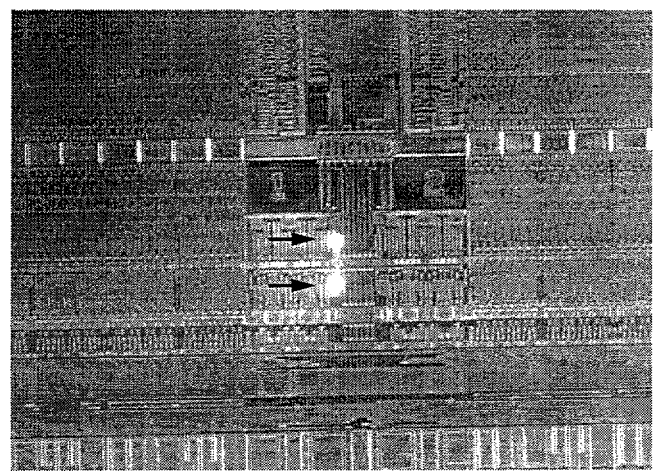

Fig. 3 - Overlay of FMI and reflected light images showing the locations of heat-generating defects of the failed SRAM in example 1.

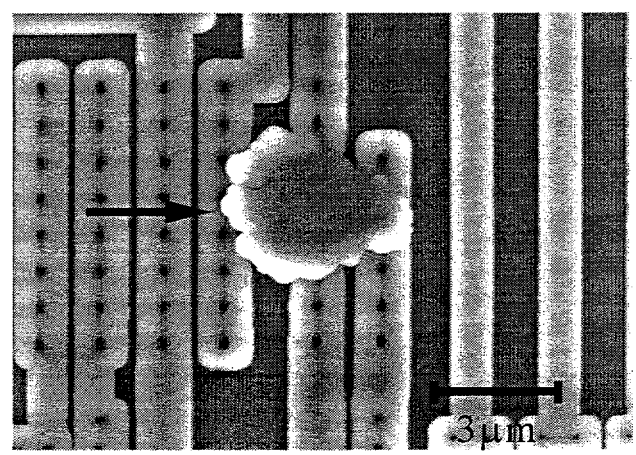

Fig. 4 - SEM image showing an embedded particle that produces an ohmic short between two adjacent metal lines.

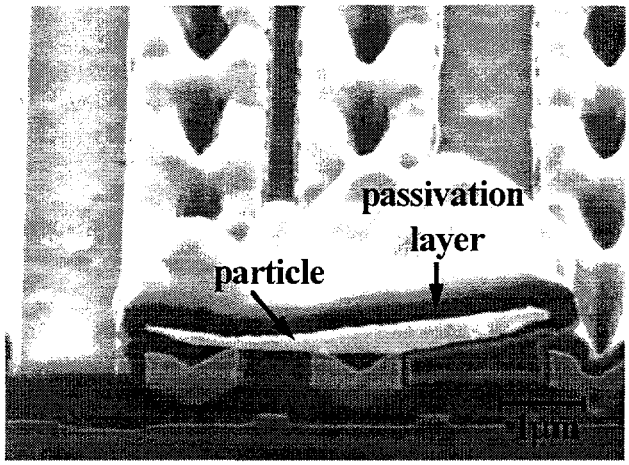

Fig. 5 - FIB cross section of the embedded particle shown in Fig. 4.

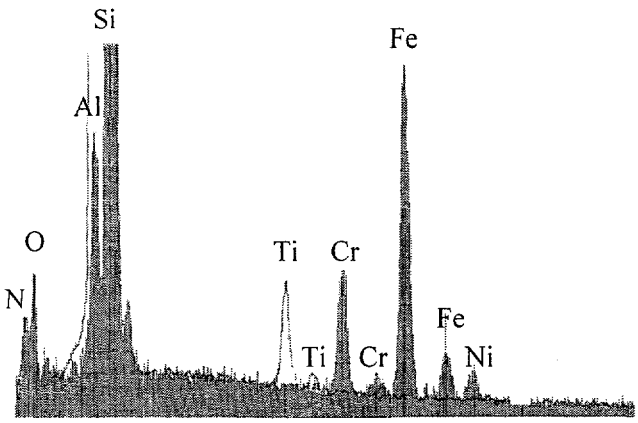

Fig. 6 - EDX spectra of the embedded particle shown in Fig. 4 and the adjacent metal line.

Example 2. The second example is another 1-megabit SRAM that has the same layout and functional operating characteristics as the SRAM described in example 1. This SRAM failed the functional test after an elevated voltage stress and had an elevated I_{DDQ} of 5 mA at 5 V. The I-V curve of this IC is shown in Fig. 7 and it is different from that shown in Fig. 2 in two respects. First, I_{DDQ} increases greatly when V_{DD} is above 1.6 V (versus 1 V for Fig. 2). Second, the curve does not have a single linear region above 1.6 V. The I-V curve strongly suggests that the failure of this SRAM involves more than just a simple ohmic short and most likely involves other processes such as those that cause light emission. In fact, three light-emitting areas were located in this IC (Fig. 8(a)). A heat-generating area was also located with FMI. The locations of the light-emitting and heat-generating areas, however, did not coincide. Upon further SEM examination (Fig. 9) and visual inspection, the root cause of the failure was determined to be an embedded particle that was identified using FMI (Fig. 8(b)). The particle produced an ohmic short between two adjacent metal lines. By design, one of these

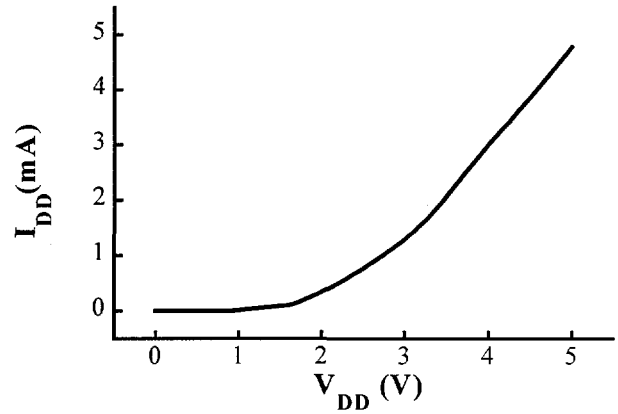

Fig. 7 - I_{DDQ} versus V_{DD} for the failed SRAM in example 2.

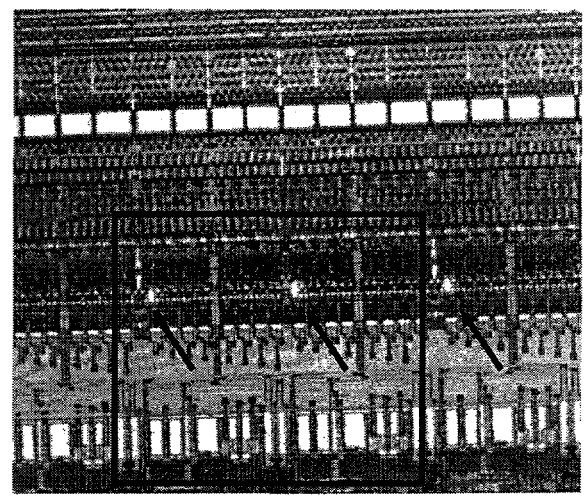

8(a)

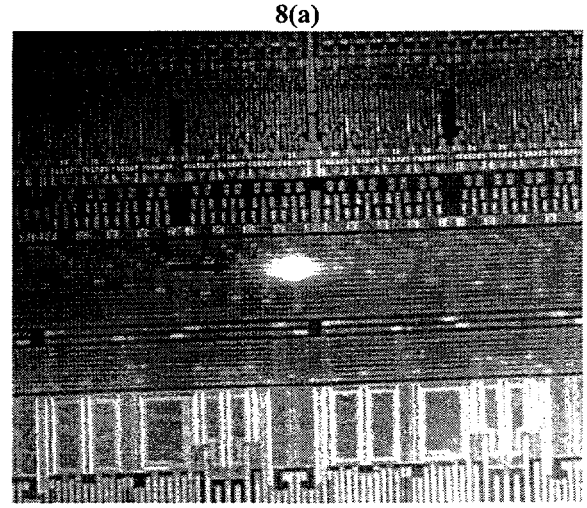

8(b)

Fig. 8 - 8(a), overlay of light-emission and reflected light images showing light-emitting regions of the failed SRAM in example 2; 8(b), overlay of FMI and reflected light images showing the location of a "hot spot". The black rectangular outline in 8(a) indicates the area where the FMI image in 8(b) was taken.

metal lines was electrically connected to the gates of several transistors in series. The ohmic short caused these transistors to go into saturation, resulting in light emission.

Example 3. The third example is an SRAM similar to those described in examples 1 and 2. This SRAM failed the functional test after an elevated voltage stress and had an elevated I_{DDQ} of 18 mA at 5 V. The I-V curve of this IC (Fig. 10) has a linear region and passes through the origin. This IV characteristic indicates that there is a direct ohmic short between V_{DD} and V_{SS}. Using FMI, a "hot spot" (Fig. 11) was located in this IC. Interestingly, this "hot spot" also emitted light. Upon further visual inspection, the root cause was identified to be *pn* junction damage in one of the input protection diodes, producing a resistive short of 200 Ω (estimated from the I-V curve) between V_{DD} and V_{SS}.

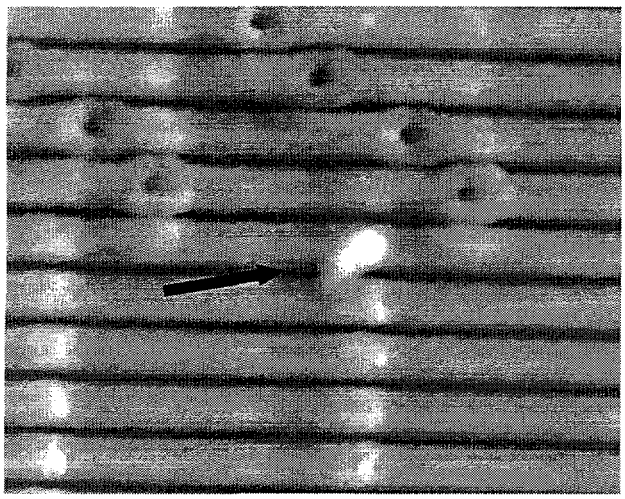

Fig. 9 - SEM image showing an embedded particle that produces an ohmic short between two adjacent metal lines in the failed SRAM in example 2.

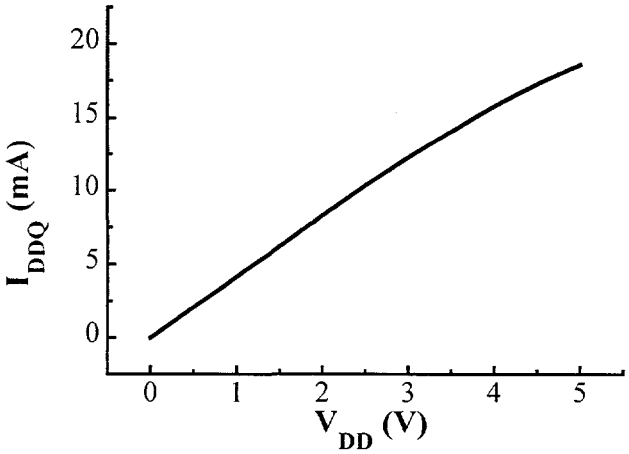

Fig. 10 - I_{DDQ} versus V_{DD} for the failed SRAM in example 3, showing a linear region that passes through the origin.

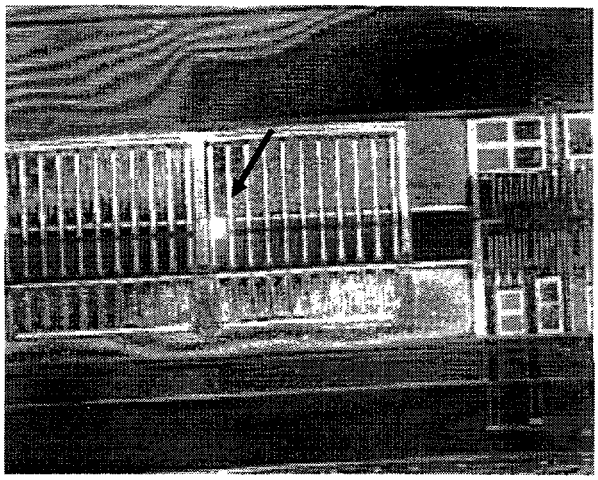

Fig. 11 - Overlay of FMI and reflected light images showing the location of a heat-generating defect of the failed SRAM in example 3.

Example 4: The fourth example involves failure of an assembly test chip (ATC) designed for measurement of mechanical stress and thermal resistance. The ATC was fabricated using a 2 μm twin-tub CMOS technology with two levels of metal. After fabrication, a functional test was performed on this ATC and it was found that one of the ring oscillators failed functionally. Using FMI, two heat-generating areas were located in the output buffer region (Fig. 12). Upon visual inspection, mechanical damage was found near the heat-generating areas (Fig. 13). This mechanical damage produced an open circuit in the metal line that connected the gates of several transistors to a driving circuit. The floating gates, in turn, caused the transistors to go into saturation, resulting in heat generation.

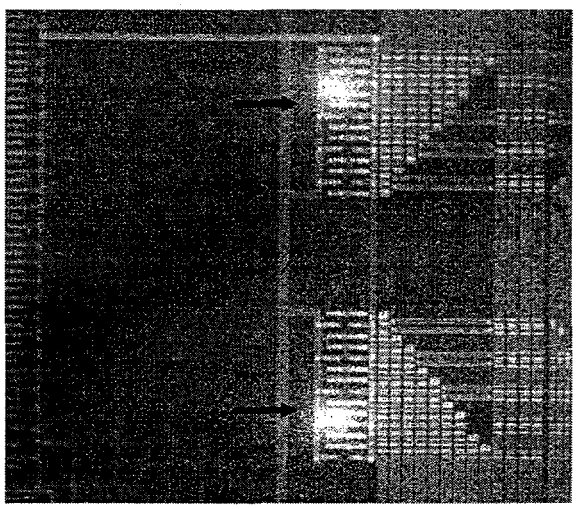

Fig. 12 - Overlay of FMI and reflected light images showing two heat-generating areas of the failed IC in example 4.

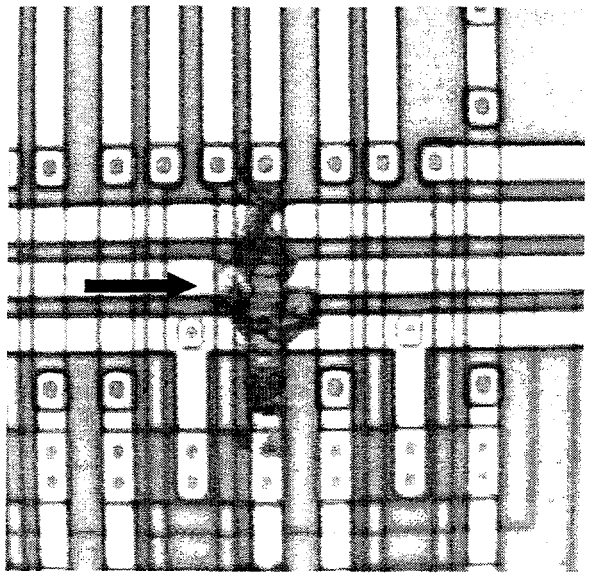

Fig. 13 - Optical image showing mechanical damage near the heat-generating areas in Fig. 12.

Example 5: The fifth example involves failure of a 256k-bit SRAM. The 64k x 8 SRAM was fabricated using a 0.5 μm N-well CMOS technology with three levels of metal. It has a nominal operating voltage of 3.3 V and a nominal standby I_{DDQ} of < 200 μA. After packaging, a functional test was performed on this SRAM and it failed functionally and had a high I_{DDQ} of > 100 mA at 3.3 V. The I-V curve of this IC showed a linear region, indicating an ohmic short. FMI was used to locate the heat generating area (Fig. 14). Temperature information derived from the FMI image (equation 1) showed that there was an average rise of ~ 2 °C above room temperature in the background surrounding the heat-generating defect. On the other hand, an average rise of ~ 3.5 °C above room temperature was observed within the heat-generating area. The temperature information indicates that the defect is not a localized heat source. Upon visual inspection, a patterning defect was observed at the heat-generating area (Fig. 15). FIB cross section (Fig. 16) shows that part of the oxide layer is missing in the heat-generating area, resulting in a direct electrical contact between several polysilicon lines and the silicon substrate. The silicon substrate has high thermal conductivity and this explains why there is a significant rise in the background temperature surrounding the defect.

Example 6: The final example also involves the failure of a 256k-bit SRAM. The SRAM has the same layout and functional operating characteristics as described in example 5. This SRAM was part of a low-yield lot that failed functionally and had a high I_{DDQ} of > 100 mA at 3.3 V. The I-V curve of this device also showed a linear region that passed through the origin, indicating an ohmic short. No light emission was detected in this device. FMI was used to quickly locate the heat generating area (Fig. 17). The FMI image in Fig. 17 shows not only the location of the hot spot but also the current paths leading to it. Upon visual inspection, the root cause of this failure was determined to be a metal 1 patterning defect (Fig. 18) which produced an ohmic short between V_{DD} and V_{SS}.

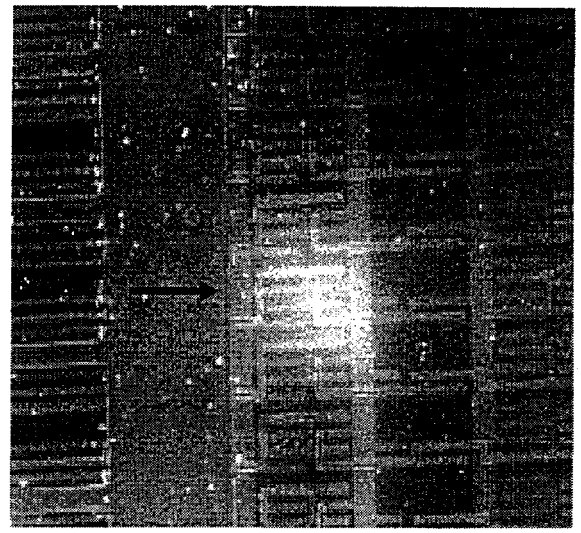

Fig. 14 -Overlay of FMI and reflected light images showing a heat-generating area in the failed SRAM in example 5.

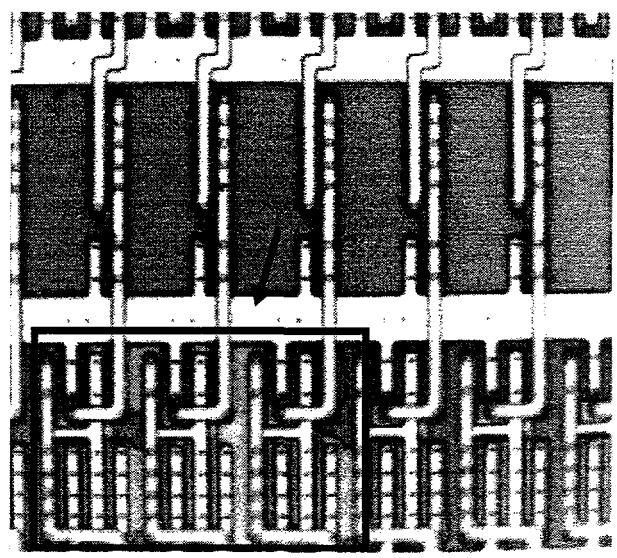

Fig. 15 - Optical image showing a patterning defect in the failed SRAM in example 5. The black rectangular outline indicates the boundary of the defect.

FMI Sensitivity

In this section, we describe the use of a failing IC to demonstrate the sensitivity of FMI (the lowest power that can

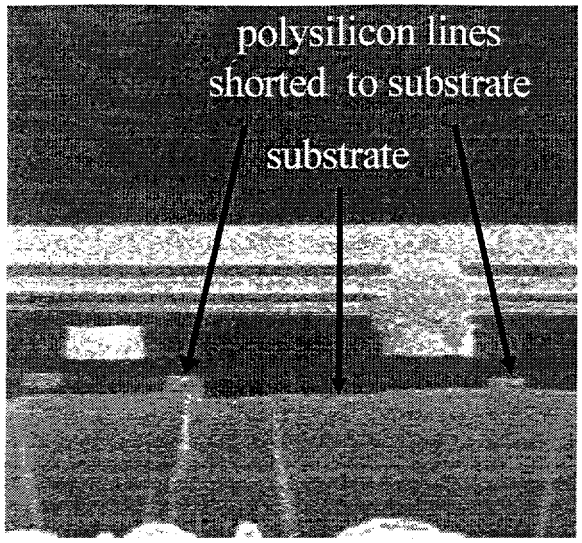

Fig. 16 - FIB cross section of the heat-generating area in the failed SRAM in example 5.

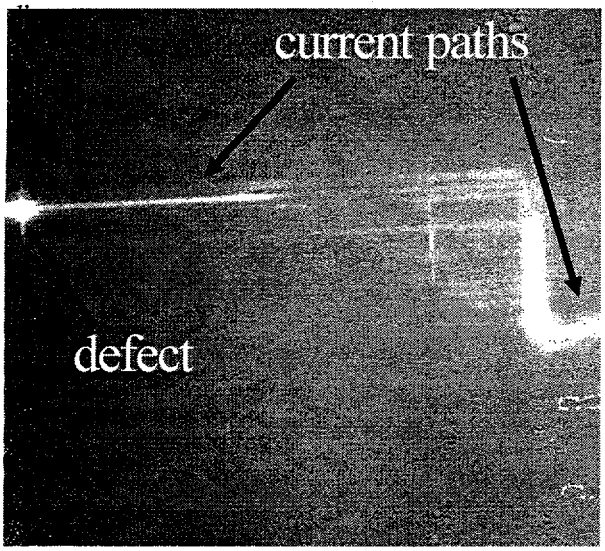

Fig. 17 - FMI image showing a heat-generating defect as well as several current paths leading to it for the failed SRAM in example 6.

be detected). This IC was an SRAM and of the same type described in example 1. It failed functionally after an elevated voltage stress with an elevated I_{DDQ}. The root cause of this failure was determined to be an embedded particle with a diameter of ~ 4 μm and thickness of ~ 0.5 μm (Fig. 19). This IC was chosen because it represented an ideal situation for FMI technique; i.e., the heat-generating defect was a very localized, was near the surface, and had a very high power density. The power density of this defect at 5 V and 600 μA (3 mW) was calculated to be ~ 1 x 10^8 W/cm^3. To analyze the sensitivity, the power to the IC was gradually lowered and FMI images were recorded. Fig. 20 shows the FMI images

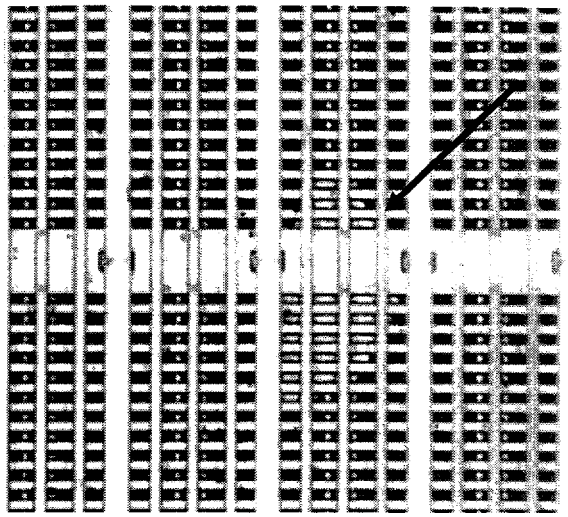

Fig. 18 - Optical image showing a metal 1 patterning defect in the failed SRAM in example 6.

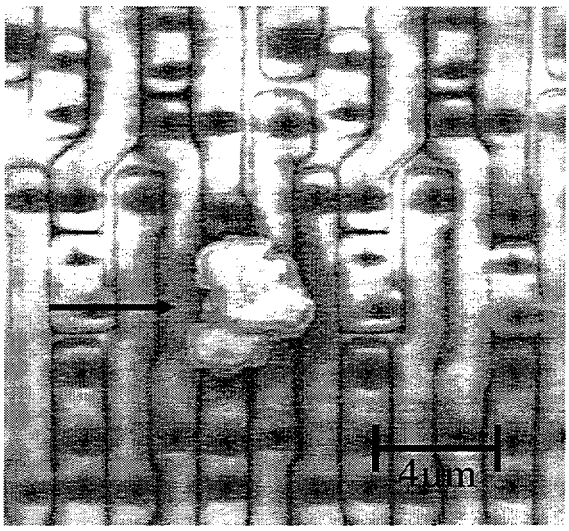

Fig. 19 - SEM image showing the size of an embedded particle in the failed SRAM used for FMI sensitivity analysis.

at different power levels while Fig. 21 shows the temperature profiles across the defect at each power level. The hot spot was detectable using FMI imaging down to about 300 μW of power. From the temperature profiles, the thermal noise was determined to be approximately 0.1 °C. The FMI images in Fig. 20 were taken with single-frame acquisition and no averaging. With signal averaging, sensitivity should improve by at least a factor of two. A more uniform coating of the EuTTA-based films onto the sample (for example by spinning) should also improve the sensitivity by another factor of two. As a result, it is estimated that the ultimate sensitivity of FMI in an ideal condition to be ~ 80 μW and thermal noise to be ~ 0.03 °C.

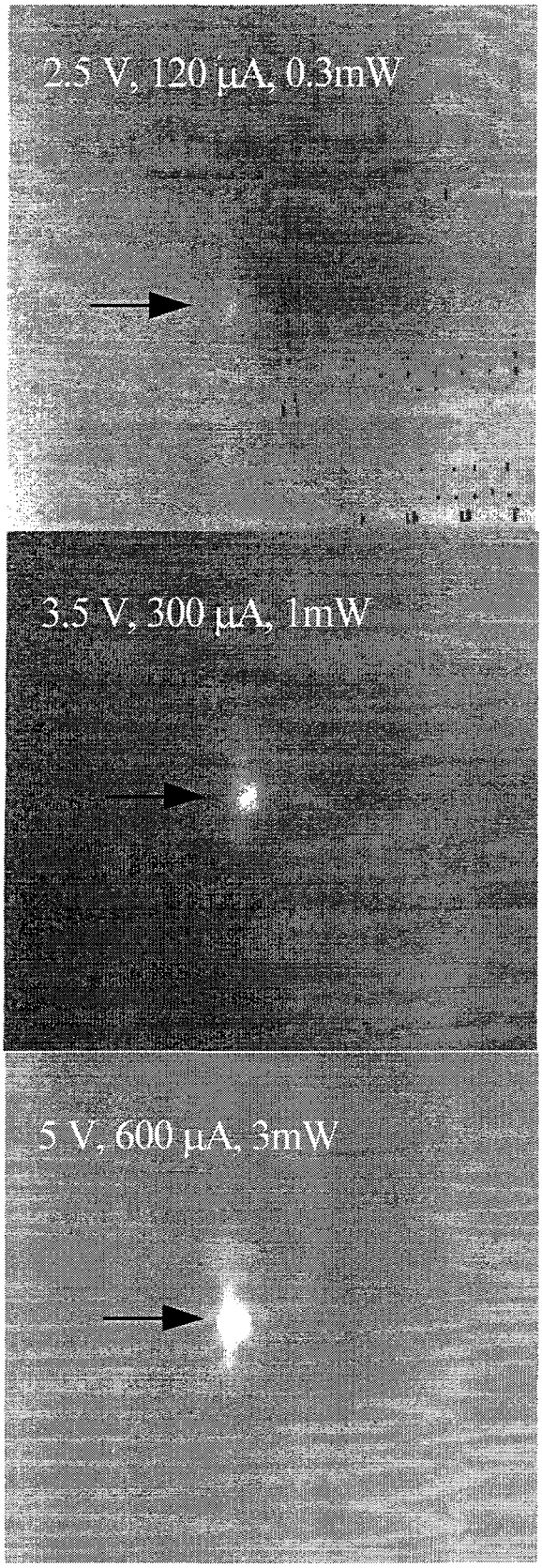

Fig. 20 - FMI images showing the heat-generating defect of the failed SRAM at different power levels.

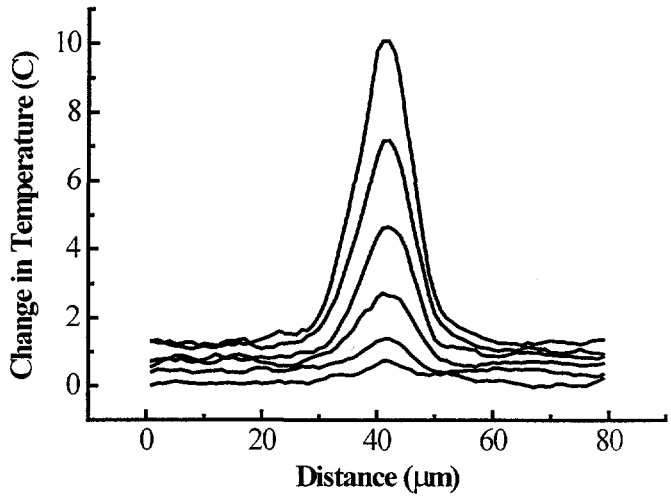

Fig. 21 - Temperature profiles across the heat-generating particle at power levels of 0.3, 0.6, 1, 1.6, 2.3 and 3 mW.

Conclusion

In this paper, we present several examples of different types of failure modes and mechanisms where FMI quickly localized the heat-generating defects. We also demonstrate that FMI is a valuable tool when used with other failure analysis techniques to efficiently identify the root cause of failures in complex ICs. In addition, we estimate the ultimate sensitivity of FMI to be ~ 80 µW in an ideal situation where the defect is localized, is near the surface, and has a high power density.

Acknowledgments

The authors would like to thank Richard E. Anderson and Edward I. Cole for reviewing this manuscript. We are also grateful to Jim Rife for his help with FIB cross sectioning. This work was performed at Sandia National Laboratories and is supported by the U.S. Department of Energy under contract DE-AC04-94AL85000.

References

1. P. Kolodner and J. A. Tyson, "Microscopic Fluorescent Imaging of Surface Temperature Profiles with 0.01 °C Resolution," *Appl. Phys. Lett.* **40**, 782 (1982).
2. P. Kolodner and J. A. Tyson, "Remote Thermal Imaging with 0.7 mm Spatial Resolution using temperature-dependent Fluorescent Thin Films," *Appl. Phys. Lett.* **42**, 117 (1983).
3. H. Winston, O. J. Marsh, C. K. Suzuki, and C. L. Telk, "Fluorescence of Europium Thenoyltrifluoroacetonate. 1:

Evaluation of Laser threshold Parameters," *J. Chem. Phys.* **39**, 267 (1963).

4. M. Bhaumik, "Quenching and Temperature Dependence of Fluorescence in rare-earth Chelates," *J. Chem. Phys.* **40**, 3711 (1964).
5. G. Crosby, R. Whan, and R. Alire, "Intramolecular Energy Transfer in Rare Earth Chelates. Role of the Triplet State," *J. Chem. Phys.* **34**, 743 (1961).
6. E. Bowen and J. Sahu, "The Effect of Temperature on Fluorescence of Solutions", *J. Phys. Chem.* **63**, 4 (1959).
7. P. Kolodner, A. Katzir, and N. Hartsough, "Noncontact Surface Temperature Measurement During Reactive-Ion Etching using Fluorescent Polymer Films,"*Appl. Phys. Lett.* **42**, 749 (1983).
8. D. L. Barton, "Fluorescent Microthermographic Imaging," *Proc. of the 20th ISTFA*, 87 (1994).
9. V. J. Bruce, "Comparison of Fluorescent Microthermography to other Commercially Available Techniques," *Proc. of the 20th ISTFA*, 73 (1994).
10. P. Tangyunyong and D. L. Barton, " Photon Statistics, Film Preparation and Characterization in Fluorescent Microthermal Imaging," *Proc. of the 21st ISTFA*, 79 (1995).
11. D. L. Barton and P. Tangyunyong, "Fluorescent Microthermal Imaging - Theory and Methodology for Achieving High Thermal Resolution Images," *Microelectronics Engineering* **31**, 271 (1996).
12. J. M. Soden and C. F. Hawkins, "I_{DDQ} Testing and Defect Classes - A Tutorial," *Custom Integrated Circuits Conf.*, 633 (1995).